Modeling multilayered wire strands, a strategy based on 3D finite element beam-to-beam contacts - Part II: Application to wind-induced vibration and fatigue analysis of overhead conductors

Sébastien Lalonde[a], Raynald Guilbault[b], Sébastien Langlois[c]

[a, c] *Université de Sherbrooke, Faculty of Engineering, Department of Civil Engineering, Sherbrooke, Canada*
[b] *École de technologie supérieure, Department of Mechanical Engineering, Montréal, Canada*

Abstract

Wind-induced loads cause electrical transmission line fatigue. Evaluation procedures consider descriptors such as deflection amplitude (Y_b) and far-field vibration (fy_{max}), which cannot relate endurance limits and wire loads. The investigation uses the finite element (FE) strategy developed in part I to study Aluminum Conductor Steel Reinforced (ACSR) submitted to wind-induced loads. The analysis underlines the Y_b and fy_{max} discrepancies. A factorial design leads to a model relating them with a precision of 92%. Comparisons with experimental ACSR data indicate that fatigue predictions from the Coffin-Manson relation associated with the FE model provide realistic evaluations of service lives.

Keywords: Multilayered wire strands, Finite element modeling, Bending stiffness, Overhead ACSR conductor, Dynamic bending stress, Conductor fatigue

1. Introduction

Cyclic bending loads resulting from wind-induced vibrations near restraining fixtures may compromise the integrity of cable-supported structures [1,2]. They also particularly affect overhead electrical transmission lines [3]. In fact, Aeolian vibrations are among the main causes of conductor fatigue damage in transmission lines [4]. Hence, a careful evaluation of their impacts on local stress distributions represents an essential exercise. However, predicting the load severity is a complex endeavor as stranded assemblies involve multiple wire contact interactions [5].

The present study exploits the finite element modeling strategy developed and validated in Part I of this two-paper series [6] to analyze the response of wire strands submitted to cyclic bending loads. Although the study focuses on ACSR (Aluminum Conductor Steel Reinforced) conductors, the proposed methodology applies to most wire strand bending problems.

In overhead conductor assemblies, severe cyclic bending loads occur near suspension clamps, vibration dampers and spacer-damper arms. At these locations, bending loads generate fretting fatigue at contact interfaces [7], and consequently, have detrimental effects on conductor service life. To estimate the dynamic load severity associated with specific vibration levels, industry standards consider fatigue indicators such as the alternating bending stress (σ_a) evaluated at the topmost

outer layer wire [4,8]. The evaluated dynamic stress must be lower than the endurance limit of the conductor measured during experimental vibration fatigue tests [4].

Because the geometry of the conductor is complex, σ_a is very hard to encapsulate in an analytical formulation. Thus, σ_a is still commonly estimated through a simplified model proposed by Poffenberger and Swart [9] [10]. This approach reduces the conductor/clamp configuration to a simple cantilever beam undergoing cyclic reversed deflection at its free end while being submitted to a tension load. This model neglects all internal friction effects, and considers that each wire bends independently. The Poffenberger-Swart model therefore uses a minimal theoretical flexural stiffness (EI_{min}) or a lower bound of σ_a. This approach leads to significant underestimations of real dynamic stresses. This is especially true when vibration amplitudes are small, since under small movements, the strand wires tend to act as a solid beam.

While the literature proposes several analytical and semi-analytical models [5,11], none of them has gained general approbation from the field industry to date. This is due in part to the fact that each of the models is based on different simplifying assumptions, which do not match all situations. For example, Giglio and Manes [12] made use of the analytical thin-rod formulation proposed by Costello [13] and ignored inter-wire friction to predict the fatigue life of wire ropes subjected to axial loads. In their study, Argatov et al. [14] addressed the bending over sheave fatigue wear of wire ropes using a model based on Archard law in which the influence of strand kinematic on wire local stresses was simply omitted.

Modern computer capacities now allow the development of more efficient numerical tools for multilayered wire strand analysis. Through a 3D discretization of each wire with beam elements, the modeling strategy put forward in Part I [6] avoids most of the above common simplifying assumptions, and all types of inter-wire contact interactions are integrated via a line-to-line contact algorithm.

After a brief summary of the prevailing analytical formulations in Section 2, Section 3 of this second part of the paper series compares predicted dynamic deflection values with published experimental results, and demonstrates the precision of the modeling strategy in Part I. Next, Section 4 develops and validates a tool based on a factorial design establishing the connection between the standard stress parameters used in practice to assess the load severity. Section 5 describes the influence of the internal friction forces on alternating stress (σ_a). Finally, Section 6 integrates the σ_a FE model predictions into a fatigue damage analysis to obtain a direct assessment of the bending load severity.

2. Theoretical approach

To facilitate comparison, the following briefly presents the analytical estimation approach of σ_a.

The σ_a formulation proposed by Poffenberger and Swart [9] considers a straight conductor with fixed ends, submitted to standing wave vibrations (Fig. 1). It also assumes that close to its fixed ends, the conductor deflection departs from the assumed sine shape; the deflection curve asymptotically progresses from a horizontal line (at the clamped end) to a sine-shape loop section (Fig. 1).

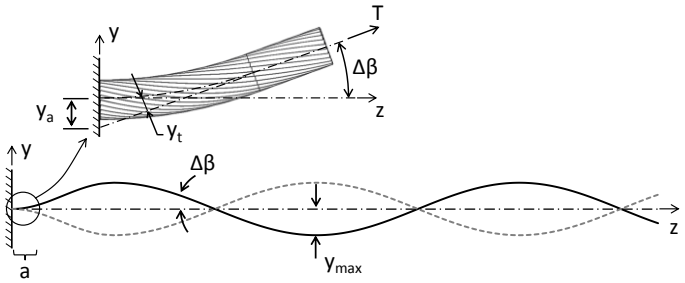

Fig. 1 - Schematization of conductor standing wave vibrations (reproduced from EPRI (2006))

Eq. (2.1) defines the strand curvature, while neglecting inertial forces. In this equation, the bending moment (M) results from the multiplication of the axial tension (T) and the departure of the conductor deflection from the sine-shape loop (y_t).

$$\frac{d^2 y_t}{dz^2} = \frac{M}{EI} = \frac{T}{EI} y_t \tag{2.1}$$

For large z values, y_t tends to zero. The solution to eq.(2.1) thus becomes $y_t = Ae^{-\sqrt{(T/EI)}z}$, where A is a constant expressed as

$A = \dfrac{y(z)}{e^{-\sqrt{T/EI}\,z} - 1 + \sqrt{T/EI}\,z}$ [15]. On the other hand, at z = 0 the conductor slope (dy_t/dz) is Δβ (Fig. 1). Therefore, assuming small deflection angles, the deflection becomes $y(z) = -y_a + \Delta\beta z + y_t$ [15]. Combining these relations into eq. (2.1) leads after some simplifications to the expression given by eq. (2.2) [15].

$$\left(\frac{d^2 y_t}{dz^2}\right)_{z=0} = \left(T/EI\right) A \tag{2.2}$$

where y is the conductor deflection amplitude measured at a distance $z \le a$ (Fig. 1). The approach considers independent wires i, and therefore uses a lower bound of the strand bending stiffness (EI) (eq. (2.3)).

$$EI = \sum_{i=1}^{i=nb\,wire} E_i I_{0i} \tag{2.3}$$

E_i is the Young modulus of the wire i material, and $I_{0i} = \pi d_i^4/64$ for round wires of diameter d_i. With the conductor curvature defined by eq. (2.2), it is then possible to determine the bending stress level (σ_a) at the strand fixed end ($z = 0$).

2.1. Y_b method

To standardize industry practice, an IEEE committee in 1966 proposed the establishment of a conductor vibration intensity from peak-to-peak deflection (2_y), measured at 89 mm (3.5 in) from the clamp exit (Fig. 2). This deflection measure is identified as the Y_b parameter.

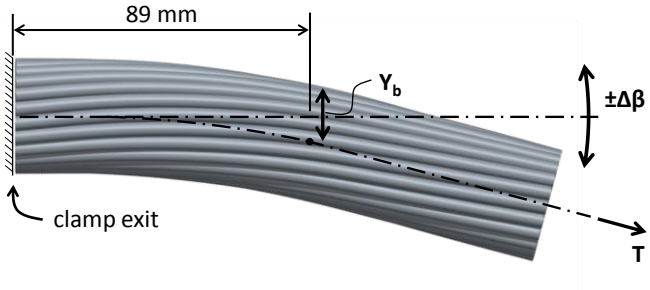

Fig. 2 - Standardized conductor dynamic bending amplitude measurement

Integrating Y_b into eq.2.2 leads to eq. (2.4) also known as the *Poffenberger-Swart Formula* (PS) [9], where d_c is the conductor diameter and z = 89 mm. Eq. (2.4) establishes the alternating bending stress σ_a. The variable E_a represents the Young modulus of the external layer wire material.

$$\sigma_a = \frac{d_c E_a \left(\frac{T}{4EI}\right)}{e^{\sqrt{T/EI}z} - 1 + \sqrt{T/EI}z} Y_b \tag{2.4}$$

2.2. fy_{max} method

The bending stress σ_a may also be evaluated based on the vibration frequency f and the far-field amplitude y_{max} (Fig. 1), leading to the fy_{max} parameter.

At the position where the conductor deflection adopts the sine-shape loop (Fig. 1), the slope dy_t/dx corresponds to Δβ, and may be expressed as a fy_{max} function (eq. (2.5)) [4],

$$\Delta\beta = \frac{2\pi f y_{max}}{\sqrt{T/m}} \tag{2.5}$$

where m is the conductor mass per unit length. eq. (2.1) may be redefined in terms of fy_{max}, eq. (2.6) [4].

$$\left(\frac{d^2 y_t}{dz^2}\right)_{z=0} = 2\pi\sqrt{\frac{m}{EI}} f y_{max} \tag{2.6}$$

σ_a is then given by eq. (2.7).

$$\sigma_a = \pi d_c E_a \sqrt{\frac{m}{EI}} f y_{max} \tag{2.7}$$

2.3. Theoretical endurance limits

Based on surveys of numerous experimental conductor fatigue tests, EPRI [4] established endurance limits (at 500 M cycles) for several ACSR in terms of parameters Y_b and fy_{max}.

For fy_{max} controlled fatigue tests, EPRI suggested endurance limits of 149 mm/s and 118 mm/s for single-layer and multilayer ACSR, respectively. Integrated in eq. (2.7), these limits result in a stress endurance limit σ_a of 22 MPa for both ACSR types. For fatigue tests performed with imposed Y_b values, the EPRI survey defined endurance limits of 0.5 to 1.0 mm for single-layer, and of 0.2 to 0.3 mm for multilayer, ACSR, respectively. Integrated in eq. (2.4), these evaluations lead to stress endurance limits σ_a of 22.5 MPa and 8.5 MPa for single-layer and multilayer, ACSR, respectively.

A comparison of the obtained σ_a estimates shows that the values are coherent for the single-layer ACSR, whereas for multilayer ACSR, an evident discrepancy appears between the Y_b and fy_{max} predictions. This may be attributed to the *PS* model underlying assumptions which cannot account for wire strand kinematics.

In reality, the σ_a amplitudes derived from this idealized model should only be viewed as an indicator that is well correlated with experimental measurements of conductor fatigue life [16]. Expressing the conductor fatigue performance in terms of parameters Y_b and fy_{max} is nevertheless common practice [4].

It is also worth mentioning that these evaluation approaches decouple the endurance limits from the stress causing fretting damages, and therefore, prevent a clear definition of the relationship between wind-induced vibrations and conductor fretting fatigue damages [15].

A refined conductor modeling approach should therefore be useful for obtaining σ_a estimations which better reflect the physics of the wire strand.

3. Finite element modeling approach

In the following subsection, FE modeling strategy developed in Part I is applied to the ACSR alternating bending stress problem.

3.1. Model construction

The model considers the conductor as rigidly clamped at one end. The other end undergoes fully reversed angular fluctuations of $\Delta\beta$ amplitude under a constant axial tension T (Fig. 3a).

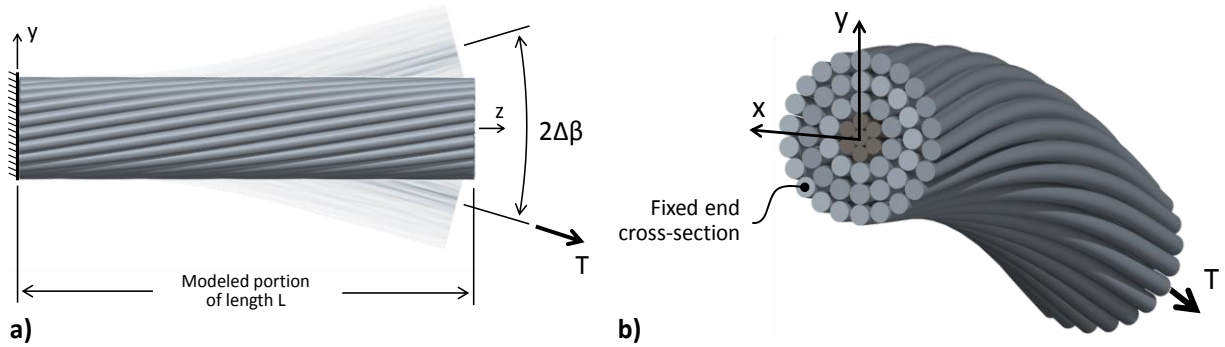

Fig. 3 - FE model configuration (a) and Wire geometric configuration at fixed end (b)

The model includes a strand section of length *L*. To facilitate the numerical-analytical σ_a comparison, the FE models are constructed such that at the fixed end, one of the wire cross-section centers of each strand layer is positioned on the *y*-axis (Fig. 3b).

3.2. Boundary conditions and load configuration

The nodes at both end sections are fully coupled with the associated node located at the center core wire. All DOF are constrained at the fixed end, whereas at the free end, only the *x* displacements and rotations about the *z*- and *y*-axes are blocked. The axial load (*T*) is first applied in the horizontal direction. The Aeolian vibrations are then introduced through reorientations of *T* at ±Δβ. Angular variations of Δβ are defined in terms of fy_{max} using eq. (2.5). They are gradually induced by increments of 0.1°. Finally, two deflection cycles are simulated in order to achieve a stabilized hysteresis loop (as defined in Part I).

3.3 Modeled ACSR

The following analysis considers four ACSR strands. The general and stranding properties of the studied conductor are given in Table 1 and Table 2, respectively [17]. In all simulations, the strand length *L* is fixed at 1000 mm.

Table 1 - ACSR general properties

Properties	ACSR 1/0	Drake	Crow	Bersfort
RTS (kN)	19.5	140.1	117.2	180.1
m (kg/m)	0.216	1.628	1.369	2.370
$E_{alum.}$ (GPa)	69	69	69	69
E_{steel} (GPa)	207	207	207	207
EI_{min} (Nm²)	3.9	43.4	18.1	61.6
EI_{max} (Nm²)	24.5	1495	1146	3827

Table 2 - ACSR stranding properties

Layer	n_i	d_i (mm)	E (GPa)	α_i (°)
ACSR 1/0				
Core	1	3.37	207	-
1	6	3.37	69	6
ACSR Drake				
Core	1	3.45	207	-
1	6	3.45	207	5.8
2	10	4.44	69	10.7
3	16	4.44	69	12.9
ACSR Crow				
Core	1	2.92	207	-
1	6	2.92	207	6.34
2	12	2.92	69	10.61
3	18	2.92	69	11.19
4	24	2.92	69	12.49
ACSR Bersfort				
Core	1	3.32	207	-
1	6	3.32	207	6.2
2	10	4.27	69	9.7
3	16	4.27	69	10.7
4	22	4.27	69	11.7

3.4 Inter-wire contact modeling

The investigation presented in Part I revealed that while a constant coefficient of friction distribution (μ_a) offers reliable numerical results, a refined friction model considering the friction coefficient variability and orthotropicity improves the numerical prediction fidelity to experimental measurements. However, in order to minimize the influence of particular modeling adjustments on the results, and also because determining the exact coefficient of friction distributions for ACSR strands submitted to wind-induced loads would be beyond the scope of the present study, the following analysis only considers constant and isotropic friction coefficients.

Therefore, μ_a is set to 0.5 for aluminum-aluminum and aluminum-steel contacts, while a value of 0.3 is applied to steel-steel contacts.

3.5. Numerical analysis of ACSR strand submitted to bending loads

This section presents and analyzes the simulation results obtained for the ACSR listed in Table 1. The study focuses on the conductor deflection and dynamic stress variations predicted close to the clamped region (fixed end).

3.6. Validation of the modeling approach

The following compares the simulation results to the experimental measurements published by Lévesque et al. [18]. In that reference paper, the authors tested three different ACSR types: Drake, Crow and Bersfort. The test bench is described in [19]). The conductors were excited at various controlled modes and y_{max} amplitudes under axial tension (T) levels

corresponding to: 15%, 25% and 35% of the conductor RTS (Rated Tensile Strength). The conductor peak-to-peak deflection amplitudes were measured at multiple locations: at 89 mm from the clamp edge (Y_b position), as well as at 45 mm (Y_{b45}), 178 mm (Y_{b178}), and 267 mm (Y_{b267}).

The experimental configurations were reproduced in the model. Fig. 3a shows the rigid fixed-end conditions integrated in the model to reproduce the square-faced clamp of the experimental system. In addition , in order to obtain precise global trends, the simulations were not limited to the tested fy_{max}, but rather, twenty $\Delta\beta$ values, ranging from 0 to about 2.0°-2.5°, were evaluated for each tension level. Fig. 4 compares the numerical solutions to the Lévesque et al.'s [18] measurements. The comparison graphs include the peak-to-peak deflection amplitudes evaluated at 45 mm (Y_{b45}), 89 mm (Y_{b89}), and 178 mm (Y_{b178}).

According to the experimental data shown in Fig. 4, the vibration mode-shape seems to have little influence on the conductor deflection close to the clamp. This observation is in line with the theory presented in Section 2.

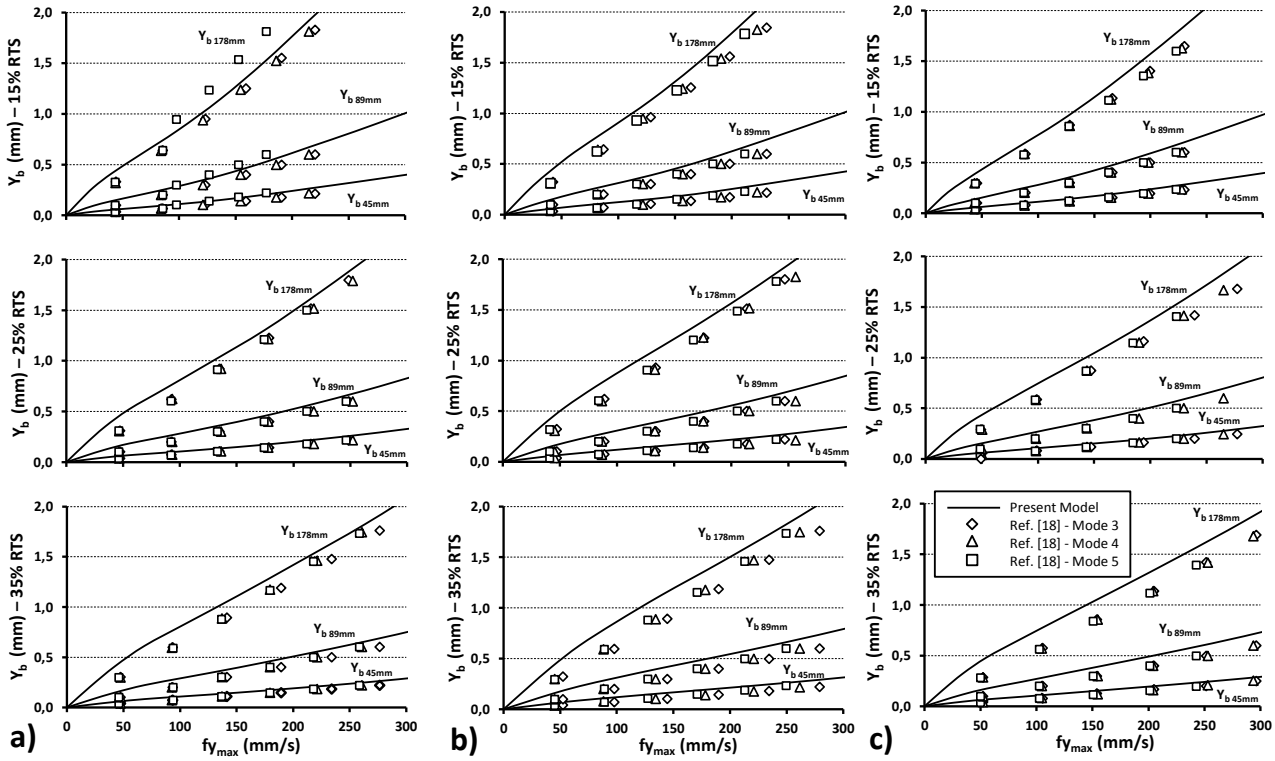

Fig. 4 - fy_{max} vs. Y_b for ACSR Drake (a), Crow (b) and Bersfort (c) at T = 15% RTS, 25% RTS and 35% RTS

The very high correspondence levels displayed in these figures confirm the validity of the proposed modeling approach. Globally, the FE model tends to slightly overestimate the conductor deflection. These differences may result from the assumed friction coefficients. Moreover, despite the apparent linear relationship between fy_{max} and Y_b demonstrated by the

experimental measurements, the higher resolution obtained with the numerical simulations rather reveal a nonlinear relation between these parameters.

4. Relation between fy_{max} and Y_b criterion

As previously mentioned, conductor fatigue performances are commonly defined in terms of fy_{max} or Y_b, since both represent measurable parameters. Therefore, depending on laboratory preferences or available equipment, fatigue curves may sometimes be defined with fy_{max} for a certain conductor model, and with Y_b for another. This often becomes unmanageable. For example, for a given strand, it might be required to access the bending load severity for known fy_{max} values, while the endurance limit is only defined for Y_b. Under such circumstances, EPRI [4] suggests experimentally determining the fy_{max} value that corresponds to the Y_b endurance limit. This test should also be performed at the Y_b endurance limit amplitude, since, as noted in Section 3, the ratio Y_b/fy_{max} does not maintain a stable linear evolution.

The proposed modeling procedure offers an attractive alternative to experimental Y_b-fy_{max} evaluations. However, the FEA model preparation and computational cost may quickly become prohibitive. It is therefore proposed to establish a Y_b predictive tool based on a factorial design approach and built on data generated with the present FE model.

The Y_b prediction model incorporates the influence of the key factors T, fy_{max} and μ_a. The role of the adhesive coefficient of friction μ_a was indeed shown to be significant in Part I. Assuming quadratic variation effects of these parameters, the model is built from a three-level (3^3) factorial design. The selected factor T levels correspond to the usual fatigue data ranges [4]. On the other hand, the μ_a levels refer to values examined in Part I. For optimal Aeolian vibration coverage, the fy_{max} range goes from 10 to 600 mm/s. Finally, to account for the Y_b curvature changes shown in Fig. 4, the fy_{max} interpolation space is further subdivided into two sub-domains (Ω_1, Ω_2). This subdivision improves the precision of the prediction model. Table 3 presents the factors and the corresponding levels for each Ω_i.

Table 3 - Factors and levels for the interpolation domains (Ω)

Ω	Levels	Factors		
		T (% RTS)	fy_{max} (mm/s)	μ
Ω_1	1	15%	10	0.5
	2	25%	67.5	0.7
	3	35%	125	0.9
Ω_2	1	15%	125	0.5
	2	25%	362.5	0.7
	3	35%	600	0.9

All factor combinations presented in Table 3 were simulated with the FE model described in Section 3. Considering each Y_b numerical solution as exact, the formulation of the prediction equation can be established based on Lagrange polynomial

shape functions, leading to eq. (4.1). Table 4 gives the eq. (4.1) coefficients c_i for Ω_1 and Ω_2 including three ACSR: Drake, Crow and Bersfort. Simulations conducted for the single-layer ACSR 1/0, demonstrated that the friction coefficient magnitude has no effect on the conductor deflection (Y_b). Fig. 5a presents the model prediction for μ_a = 0.5 and μ_a = 0.9. This plot shows that the estimates are perfectly matching. In contrast, Fig. 5b shows the presence of interactions between T and fy_{max}.

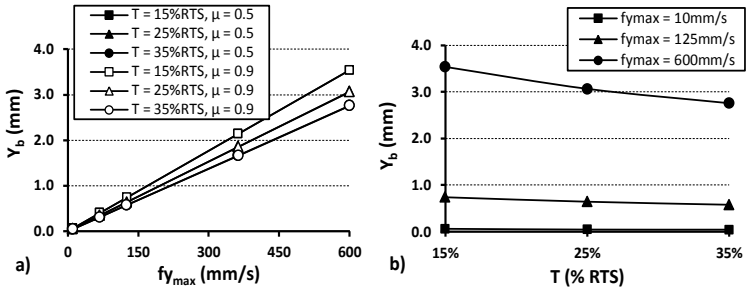

Fig. 5 – Single-layer ACSR 1/0 Y_b variation with (a) fy_{max} and (b) T

Based on these observations, a two-factor factorial design (3^2) considering a single fy_{max} interpolation space between 10 and 600 mm/s appears to be better adapted. Table 5 presents the factors and the associated levels. The Y_b prediction equation reduces to eq. (4.2). Finally, Table 6 gives the c_i coefficients.

$$\begin{aligned} Y_b\left(T, fy_{max}, \mu\right) = {} & c_0 + c_1 T + c_2 fy_{max} + c_3 \mu + c_4 T fy_{max} + c_5 T\mu + c_6 fy_{max}\mu + c_7 T fy_{max}\mu + c_8 T^2 + c_9 fy_{max}{}^2 + c_{10}\mu^2 + c_{11} T^2 fy_{max} \\ & + c_{12} T^2\mu + c_{13} T^2 fy_{max}\mu + c_{14} T^2 fy_{max}{}^2 + c_{15} T^2 fy_{max}{}^2\mu + c_{16} T^2\mu^2 + c_{17} T^2 fy_{max}\mu^2 + c_{18} T^2 fy_{max}{}^2\mu^2 \\ & + c_{19} T fy_{max}{}^2 + c_{20} fy_{max}{}^2\mu + c_{21} fy_{max}{}^2\mu^2 + c_{22} T fy_{max}{}^2\mu + c_{23} T fy_{max}\mu^2 + c_{24} T\mu^2 + c_{25} fy_{max}\mu^2 + c_{26} T fy_{max}{}^2\mu^2 \end{aligned} \quad (4.1)$$

Table 4 – Eq. (4.1) c_i coefficients

c_i	Ω_1 (10 ≤ fymax < 125 mm/s)			Ω_2 (125 ≤ fymax < 600 mm/s)		
	Drake	Crow	Bersfort	Drake	Crow	Bersfort
c_0	4.147746E-02	-4.565770E-01	-4.362340E-02	-1.254874E-01	-2.922646E-01	-3.795748E-01
c_1	-4.723617E-01	4.332205E+00	3.313860E-01	1.507831E-01	3.452069E+00	3.678961E+00
c_2	5.100441E-03	5.369405E-02	8.102636E-03	6.203661E-03	1.551895E-03	7.534341E-03
c_3	-1.401715E-01	1.397398E+00	1.040552E-01	-3.678143E-01	2.183204E-01	3.012140E-01
c_4	-4.835680E-03	-4.787176E-01	-3.876932E-02	-1.078746E-02	1.775008E-02	-3.854482E-02
c_5	1.585521E+00	-1.317469E+01	-5.227516E-01	5.223163E+00	-6.759697E+00	-6.254691E+00
c_6	1.105159E-04	-1.510798E-01	-9.417180E-03	2.184925E-03	1.126607E-02	-6.234226E-03
c_7	-1.956418E-02	1.442860E+00	5.793084E-02	-4.654720E-02	-9.797880E-02	6.481300E-02
c_8	1.263917E+00	-8.793719E+00	-4.156919E-01	9.869259E-01	-1.115650E+01	-9.073408E+00
c_9	-1.417234E-06	-3.970819E-04	-2.789478E-05	4.427541E-07	9.539370E-06	-1.847538E-06
c_{10}	1.211421E-01	-9.532355E-01	-1.305763E-02	4.109342E-01	-3.740889E-01	-4.913690E-01
c_{11}	-8.724118E-03	9.688959E-01	4.780175E-02	-1.467713E-06	-2.523364E-02	8.485980E-02
c_{12}	-4.209011E+00	2.664189E+01	1.982775E-01	-1.142012E+01	3.149248E+01	2.159976E+01
c_{13}	7.066455E-02	-2.920210E+00	-2.335847E-02	1.074735E-01	1.171207E-01	-1.958073E-01
c_{14}	7.909762E-05	-7.987134E-03	-3.584705E-04	2.704386E-05	1.171207E-04	-1.008411E-04
c_{15}	-3.341622E-04	2.427036E-02	2.784388E-04	-1.671228E-04	-3.387239E-04	2.883350E-04
c_{16}	3.550401E+00	-1.826174E+01	7.102872E-01	8.099565E+00	-2.795063E+01	-2.028933E+01
c_{17}	-6.745032E-02	2.000862E+00	-7.388414E-02	-7.830439E-02	-3.411320E-02	1.932788E-01
c_{18}	3.288162E-04	-1.672272E-02	5.100107E-04	1.245023E-04	1.771708E-04	-2.833172E-04
c_{19}	-1.385926E-05	3.844633E-03	2.524134E-04	-6.126250E-06	-7.078006E-05	3.637259E-05
c_{20}	-2.862127E-06	1.197747E-03	4.547789E-05	-4.888257E-06	-2.555857E-05	7.396101E-06
c_{21}	5.328412E-06	-8.338755E-04	2.317406E-06	5.605670E-06	1.616382E-05	-8.763715E-06
c_{22}	8.630541E-05	-1.170395E-02	-4.095632E-04	6.936048E-05	2.122026E-04	-9.777642E-05

c_{23}	2.153838E-02	-9.861089E-01	1.165334E-02	4.002149E-02	4.845359E-02	-7.321415E-02
c_{24}	-1.355614E+00	9.007796E+00	-1.220868E-01	-4.250385E+00	7.742336E+00	7.448899E+00
c_{25}	-1.187469E-03	1.038677E-01	1.113826E-03	-3.540463E-03	-7.020385E-03	6.325457E-03
c_{26}	-9.738842E-05	8.071674E-03	-8.651218E-05	-5.998786E-05	-1.238360E-04	1.078847E-04

Table 5 - Factors and levels for the single-layer ACSR 1/0 case

Ω	Levels	Factors	
		T (% RTS)	fy_{max} (mm/s)
Ω_1	1	15%	10
	2	25%	305
	3	35%	600

Table 6 - Eq. (4.2) c_i coefficients for single layer ($10 \le fy_{max} < 600$ mm/s)

	ACSR 1/0 c_i				
c_0	3.714370E-02	c_3	-1.029715E-02	c_6	7.059738E-03
c_1	-3.401287E-01	c_4	6.386957E-01	c_7	-4.013036E-06
c_2	7.276425E-03	c_5	4.069943E-07	c_8	9.033446E-06

$$Y_b\left(T, fy_{max}\right) = c_0 + c_1 T + c_2 fy_{max} + c_3 T fy_{max} + c_4 T^2 + c_5 fy_{max}^{\ 2} + c_6 T^2 fy_{max} + c_7 T fy_{max}^{\ 2} + c_8 T^2 fy_{max}^{\ 2} \quad (4.2)$$

In order to validate the precision of the Y_b prediction equation (eqs. (4.1) and (4.2)), Table 7 and Table 8 present a validation plan testing all mid-level factor combinations.

Table 7 - Validation plan (single layer ACSR) factor values

Mid levels	Factors	
	T (% RTS)	fy_{max} (mm/s)
1	20%	157.5
2	30%	452.5

Table 8 - Validation plan (multilayer ACSR) factor values

Mid levels	Factors		
	T (% RTS)	fy_{max} (mm/s)	μ
1	20%	38.75	0.6
2	30%	96.25	0.8
3	-	243.75	-
4	-	481.25	-

These combinations were also simulated with the FE model defined in Section 3. Figures 6 and 7 compare the eqs. 4.1 and 4.2 Y_b prediction values to the FE evaluations. The graphs also include the prediction error bars.

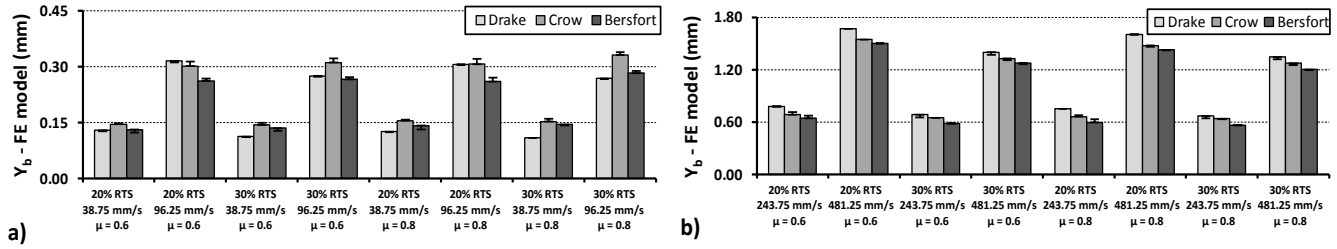

Fig. 6 - Comparison of Y_b values obtained from eq. (4.1) ((a) Ω_1 and (b) Ω_2 to FE evaluations with error bars

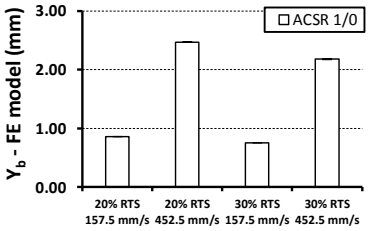

Fig. **7** - **Comparison of Y_b values obtained from eq. (4.2) (single-layer ACSR 1/0) to FE evaluations with error bars**

Compared to the FE solutions, the prediction equations (eqs. 4.1 and 4.2) demonstrate a high level of correspondence. For example, at T = 20% RTS and fy_{max} = 452.5 mm/s, eq. (4.2) (single-layer ACSR 1/0) leads to practically null deviations; the maximum error is 0.008 mm or 0.33%. On the other hand, compared to the Y_b FE solution, the maximum absolute deviation shown by eq. (4.1) (multilayer ACSR) is 0.034 mm (ACSR Bersfort at T = 20% RTS, fy_{max} = 243.75 mm/s and μ = 0.8), while the maximum relative deviation is -7.61% (ACSR Bersfort at T = 20% RTS, fy_{max} = 38.75 mm/s and μ = 0.8).

The available conductor endurance limits derived from Y_b or fy_{max} were predominantly evaluated for short radius or bell mouth commercial metallic suspension clamps (Fig. 8). On the other hand, the prediction model does not integrate the fixture shape in the simulations. Thus, the precision of the estimation obtained from eqs. 4.1 and 4.2 for practical conditions remains to be evaluated. To that end, Fig. 9 compares the Y_b prediction resulting from eq. (4.1) to experimental fy_{max}/Y_b measurements extracted from published ACSR fatigue data: Drake [19–22], Crow [23,24] and Bersfort [19,25]. Additionally, to render the friction coefficient effect on Y_b estimation more visible, Fig. 9 includes the prediction curves generated when μ_a = 0.5, 0.7 and 0.9 at the aluminum-aluminum and aluminum-steel contacts. The steel-steel contact coefficient of friction remains fixed at 0.3.

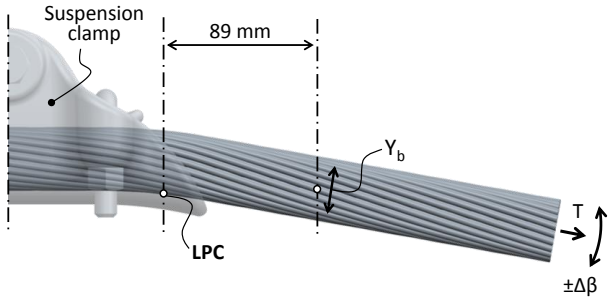

Fig. 8 - Commercial suspension clamp Y_b measurement

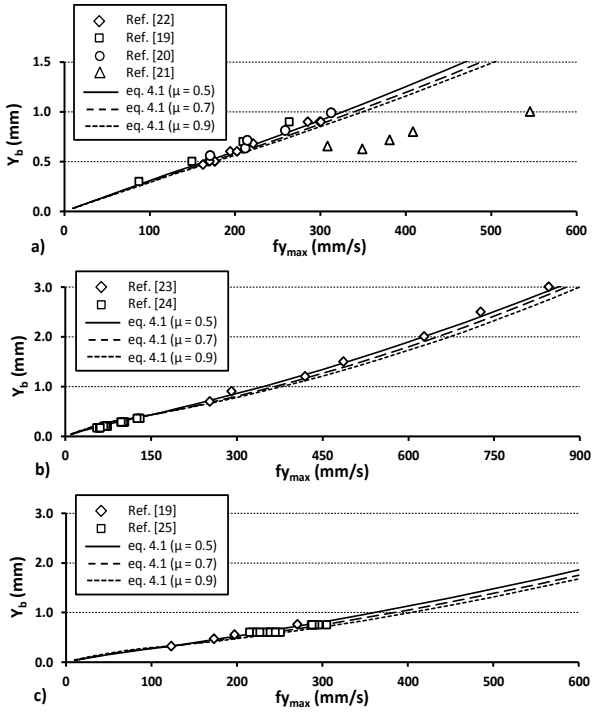

Fig. 9 - Comparison of eq. (4.1) predictions with fatigue measurement of Y_b for ACSR at the exit of short radius metallic suspension clamps: (a) Drake, (b) Crow and (c) Bersfort tensioned at T = 25% RTS

The correlations shown in Fig. 9 are excellent for all three ACSR types. Even in Fig. 9b, where the prediction results from extrapolations outside the limits of the factorial design (fy_{max} > 600 mm/s), the estimations appear to be very close to the measurements. Fig. 9 also reveals that the μ_a influence remains lower than the scattering of the experimental measurements. Therefore, it is considered that the μ_a factor may be ignored and eliminated from the factorial design. This simplification results in a unique prediction formulation given by eq. (4.2) for all ACSR types. Moreover, since the Y_b estimations made when μ_a is equal to 0.5 are slightly closer to the experimental measurements, μ_a is fixed at 0.5 at the aluminum-aluminum and aluminum-steel contacts, while the steel-steel contact coefficient of friction remains unchanged at 0.3. Table 9 gives the final eq. (4.2) c_i coefficients for the Drake, Crow and Bersfort ACSR.

Table 9 - Eq. (4.2) c_i coefficients for Drake, Crow and Bersfort ACSR when μ_a = 0.5

c_i	Ω_1 (10 ≤ fymax < 125 mm/s)			Ω_2 (125 ≤ fymax < 600 mm/s)		
	Drake	Crow	Bersfort	Drake	Crow	Bersfort
c_0	1.677219E-03	3.813032E-03	5.862408E-03	-2.066610E-01	-2.766266E-01	-3.529718E-01
c_1	-1.850450E-02	-3.191341E-03	3.144200E-02	1.699768E+00	2.007805E+00	2.426234E+00
c_2	4.858832E-03	4.121085E-03	3.656021E-03	6.411008E-03	5.429836E-03	6.009825E-03
c_3	-9.233174E-03	-3.814655E-03	-6.707037E-03	-2.405569E-02	-1.912592E-02	-2.456169E-02
c_4	4.701172E-02	-3.820740E-02	-1.194490E-01	-2.698244E+00	-2.397915E+00	-3.376851E+00
c_5	-1.516194E-06	-6.677094E-06	-4.490862E-06	-5.999570E-07	8.010386E-07	-3.559112E-07
c_6	9.745577E-03	9.006427E-03	1.720596E-02	3.415919E-02	2.479839E-02	3.557543E-02
c_7	4.946343E-06	1.057589E-05	2.505030E-05	1.355703E-05	4.362259E-06	1.462084E-05
c_8	-5.779415E-06	-3.263413E-05	-8.943414E-05	-2.539196E-05	-7.948543E-06	-2.791612E-05

Finally, considering the close agreement shown in Fig. 9 between the prediction and the experimental measurements conjointly with the original numerical model definition, which does not account for the clamping fixture shape, it may be concluded that the short clamp radius has virtually no influence on the bending response evaluated at 89 mm from the Last Point of Contact (LPC). The prediction tool formulated by eq. (4.2) and Tables 7 and 10 may thus be considered as offering reliable evaluations of the bending amplitude of conductors supported by commercial suspension clamps. This simple model provides an instant description of Y_b conditions produced by loads defined in terms of T and $fy_{max.}$

5. Dynamic bending stress analysis (σ_a)

The FE model developed in Part I can also provide immediate calculations of the alternating stress amplitude (σ_a), and thus, a direct assessment of the bending load severity via a fatigue damage analysis.

When only considering bulk stresses in configurations similar to that of Fig. 3 submitted to fatigue bending, the most solicited region of each layer appears to be at the extreme fiber of the wires close to the clamped end, and aligned with the y-axis (Fig. 10).

The following makes use of the FE model described in Section 3 to determine the σ_a variations when the four conductors of Table 1 are submitted to fluctuating Y_b amplitudes under T = 15%, 25% and 35% RTS. The σ_a evaluations describe the σ_{zz} stress differences (Fig. 10) produced by T between the two-limit angular positions –Δβ and +Δβ. The evaluation is carried out for each aluminum layer.

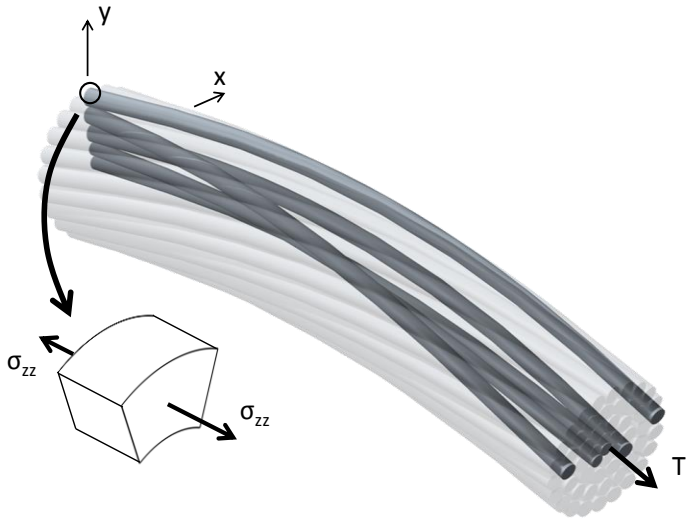

Fig. 10 - Strand orientation for dynamic bending stress (σ_a) evaluations

295 Fig. 11 to present the σ_a variations calculated for the Y_b ranging from 0 to 1 mm. The graphs also include the analytical

296 evaluations produced with eq. (2.4), assuming EI_{min} (eq. 2.3), and EI_{max}. EI_{max} is calculated with eq. (4.3) [26].

297 $$EI_{max} = \sum_{i=1}^{nb\ layer} n_i \left(E_i I_i \sin(\alpha_i) + \frac{A_i E_i R_i^2 \cos^3(\alpha_i)}{2} \right) + E_c I_c \quad (4.3)$$

298 In eq. (4.3), n_i, A_i, α_i and R_i correspond to the number of wires, the cross-section area, the lay angle, and the layer *i* radius,

299 respectively. E_c and I_c are the Young modulus and moment of inertia of the core wire.

300 A rapid inspection of the results shows that, on the one hand, the single-layer ACSR results in Fig. 11a demonstrate a

301 perfect match between the FE model and the analytical solution, considering the EI_{min} assumption, which is in agreement

302 with the theory presented in Section 2. On the other hand, the multilayered configurations reveal responses completely

303 different: for all three ACSR (Drake, Crow and Bersfort), at low Y_b amplitudes, the σ_a evaluations follow the EI_{max} assumption,

304 and progressively adopt a trend closer to EI_{min} theory as Y_b increases. The stress response evolution systematically begins at

305 lower Y_b amplitudes for the outer layer, and progresses toward the inner layers as Y_b intensifies. This process corresponds to

306 a progressive interlayer partial deadhesion, which also generates a corresponding load transfer onto the inner layers (causing

307 larger σ_a). In other words, because of the interlayer sliding, the outer layer wires start bending about their own center fiber

308 instead of respecting a group deformation about the conductor central axis.

309

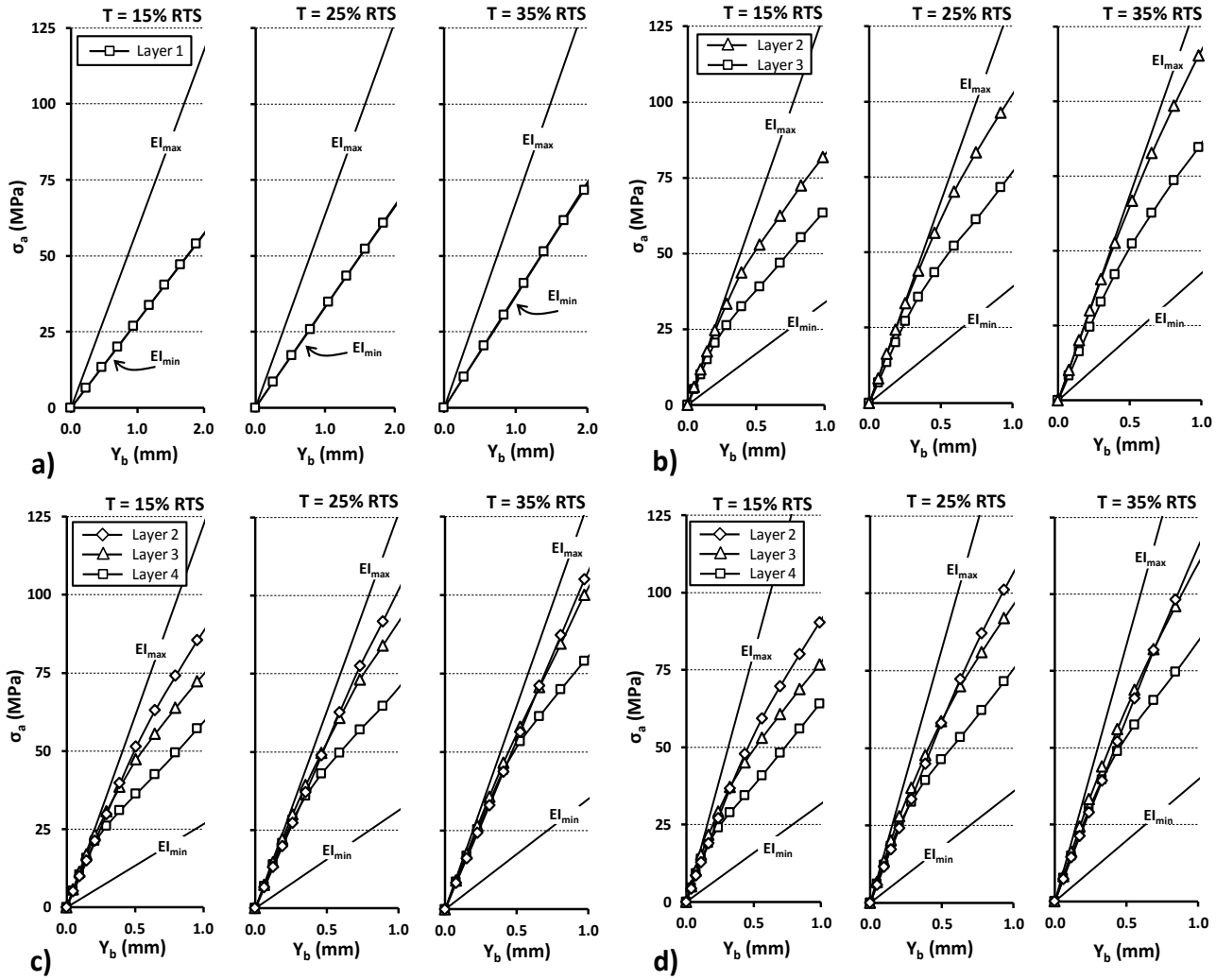

Fig. 11 - Dynamic bending stress - ACSR 1/0 (a), ACSR Drake (b), ACSR Crow (c) and ACSR Bersfort (d)

For the three analyzed multilayered ACSR, obvious signs of outer layer slip appear around Y_b amplitudes between 0.2 and 0.5 mm. Actually, a comparison of Fig. 11b) to d) shows that the exact Y_b onset level closely depends on the conductor tension (T). Higher axial tensions T engender greater normal forces at the interlayer contact points, and consequently promote the internal conductor friction forces, thus favoring the wire adhesion.

5.1 Effects of coefficient of friction (μ)

Although the results of Section 4.2 revealed a negligible effect of μ_a on Y_b, in view of the last descriptions, the situation may be different for σ_a. To illustrate the influence of μ_a on σ_a, Fig. 12 presents the variation of σ_a calculated with different μ_a values for the Drake ACSR over a Y_b range of 0 to 2 mm.

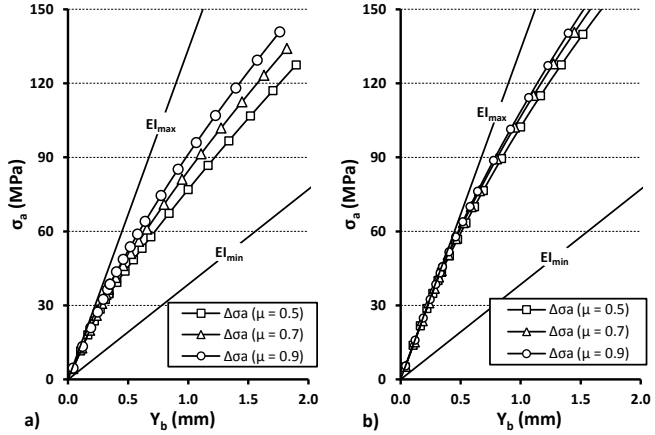

Fig. 12 - Variation of σ_a with Y_b in (a) outer layer 3 and (b) inner layer 2 for a Drake ACSR at T = 25% RTS – influence of μ_a

As expected, since larger μ_a values retard inter-wire slippage, and favor a grouped response of the conductor wires, Fig. 12a indicates that σ_a augments with μ_a increases. This graph also shows increasing effects of μ_a on σ_a with Y_b intensifications. Fig. 12b displays a similar response for the inner layer. However, because of the larger contributions of the outer layer wires conjointly provoked by μ_a and Y_b, the difference between the prediction curves is of a lesser magnitude. Finally, Fig. 12 indicates that the μ_a influence on the outer layer stress becomes significant for Y_b > 0.5 mm. Thus, the friction coefficient effect may be less significant for smaller wind-induced conductor displacements associated with Aeolian vibrations. On the other hand, the coefficient of friction role becomes more significant for galloping transmission lines.

6. Fatigue life estimation (N_f)

Because of the complexity of the problem, current practice usually estimates the conductor fatigue life based on experimental data. In an attempt to establish a universal fatigue criterion for common conductors, the CIGRÉ study committee #22 [27] proposed the σ_a Safe Border Line eq. (6.1). This semi-empirical expression relates the outer layer alternate bending stress calculated with eq. (2.4) to the number of cycles to failure (N_f). Actually, the safe line described by eq. (6.1) represents a conservative limit established from a collection of experimental measurements that were obtained through standardized fatigue tests involving conductors supported by metallic suspension clamps.

$$\sigma_a = \begin{cases} 450\left(N_f\right)^{-0.20} & for \quad N_f \le 1.56 \times 10^7 \\ 263\left(N_f\right)^{-0.17} & for \quad N_f > 1.56 \times 10^7 \end{cases} \tag{6.1}$$

The proposed FE model also offers a valuable alternative to estimate N_f. The number of cycles to failure may be calculated from the wire bulk stresses of the outer layer extracted from the numerical simulations for given Y_b values, and

integrated into any plain fatigue criterion. Obviously, this approach does not explicitly account for the fretting damage contribution.

Adopting a basic stress-life approach, the well-known Basquin relation (eq. 6.2) may be selected as the fatigue criterion. Parameters $\sigma_{f'}$ and b represent the material properties. Table 10 gives these properties for wires made of 1350-H19 aluminum [28].

$$\sigma_a = \sigma_{f'} \left(2N_f\right)^b \tag{6.2}$$

Table 10 - 1350-H19 aluminum properties

σ_y (MPa)	σ_u (MPa)	$\sigma_{f'}$ (MPa)	$\varepsilon_{f'}$	b	c
167	187	204	0.274	-0.07	-0.5

The following fatigue life evaluations consider the wire stresses calculated at the critical location of the layers illustrated in Fig. 10. Therefore, they produce fatigue life estimates N_f controlled by the failure of the first wire of the layers.

The life predictions generated with the proposed approach are compared below with several published experimental fatigue results extracted from the literature for Drake and Crow ACSR. In all cases, the conductors were tensioned at 25% of their RTS, and supported by fixed short radius metallic suspension clamps.

Fig. 13 compares the numerical/experimental fatigue life evaluations obtained for both conductors. To preserve the data presentation form adopted in the references, the graphs display the results with Y_b as the damage criterion. They include the FE model-predicted fatigue curves for the two outermost aluminum layers, the experimental data, as well as the Safe Border Line (eq. (6.1)). The reported experimental N_f correspond to cycle numbers at the first wire break. Therefore, for the sake of clarity, the graphs also indicate the wire layer of the first experimental breakage.

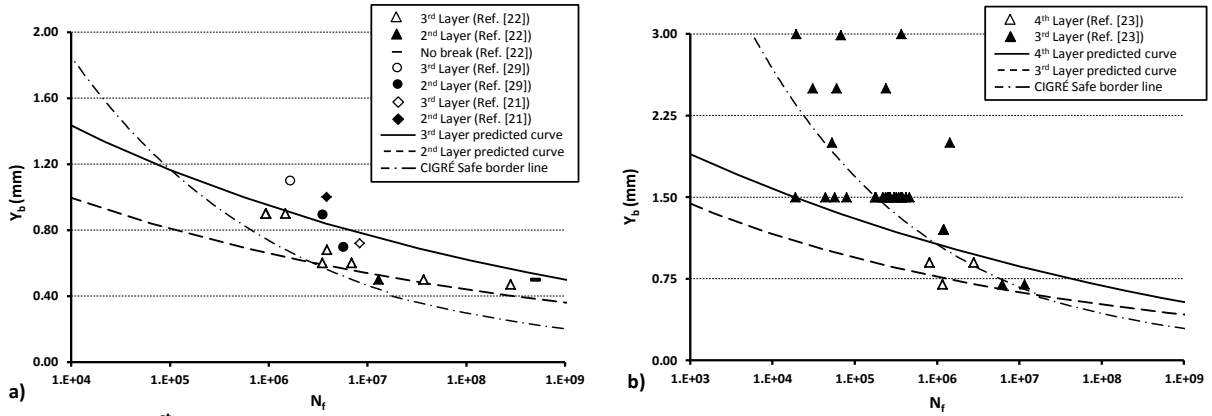

Fig. 13 - Y_b-N_f 1st break for Drake ACSR (a) and Crow ACSR (b) with prediction curves derived from the stress-life eq. (6.2)

Fig. 13 evidences the scattering present in the experimental data. In fact, this is inherent to stranded conductor experimental investigations, where any slight dimensional, positioning or load variations may significantly affect the local contact conditions. All in all, the eq. (6.2) predicted lives do not wholly reflect the general trends described by the experimental data. Actually, the FE model predictions appear to be in better agreement with the experimental data at low Y_b. On the other hand, the CIGRÉ Safe Border Line offers relatively good conductor life estimations.

Fig. 11b) and c) show that at Y_b values above 0.75 mm, σ_a becomes very significant, and may presumably cause localized plastic deformations at the different stress risers. Therefore, to improve the model and account for plastic deformation effects, it is proposed to replace the Basquin relation (eq. 6.2) with the also well-known Coffin-Manson fatigue relation (eq. 6.3). In this equation, the variable ε_a is the measured or calculated strain amplitude at the critical location, and $\varepsilon_{f'}$ and c are material parameters already introduced in Table 10:

$$\varepsilon_a = \frac{\left(\sigma_{f'}\right)}{E}\left(2N_f\right)^b + \varepsilon_{f'}\left(2N_f\right)^c \tag{6.3}$$

The Fig. 13 fatigue prediction curves were recalculated with eq. (6.3). Fig. 14 compares the new estimates with the experimental measurements and the Safe Border Line results.

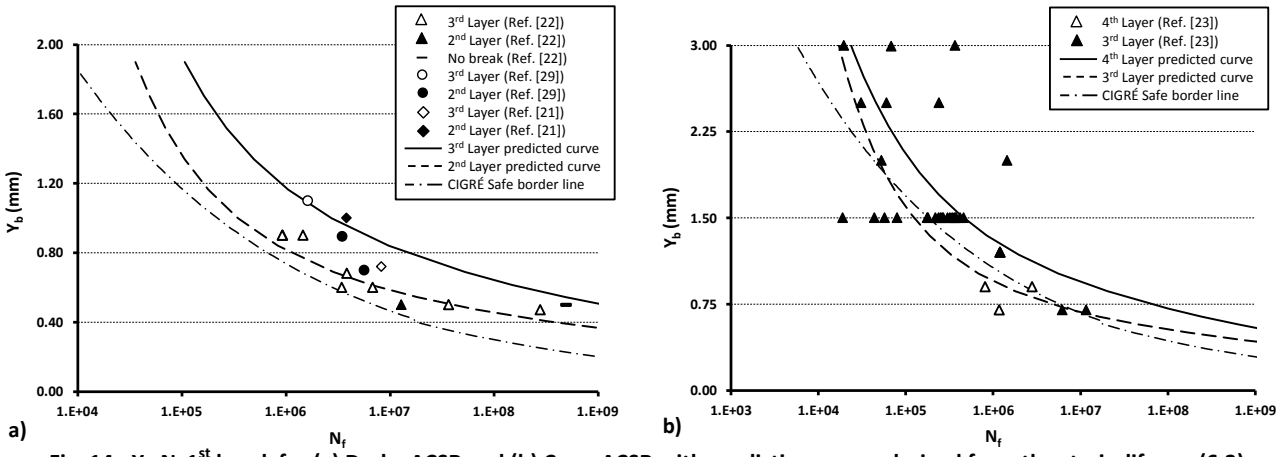

Fig. 14 - Y_b-N_f 1st break for (a) Drake ACSR and (b) Crow ACSR with prediction curves derived from the strain-life eq. (6.3)

Fig. 14 indicates that the addition of the plastic deformation effect improves the model prediction quality for both the Drake and Crow ACSR. Indeed, now the predicted life curves better correlate with the experimental measurements. In particular, the Crow ACSR graph of Fig. 14b shows that the predictions are now also excellent at very high Y_b. This is certainly an indication of the lesser role of the fretting mechanisms in fatigue damage induced under very high Y_b. In practice, high Y_b amplitudes are usually associated with galloping events.

385 The experimental data included also reveal that a majority of the first wire failure occurs at the outer layer for the Drake
386 ACSR, while it is the opposite for the Crow ACSR, where the wires of the inner layer seem to be the most susceptible to
387 fracture. This is presumably due to the lower Y_b of the fatigue test conditions maintained for the Drake ACSR, as compared to
388 the Crow ACSR. Indeed, greater deflection amplitudes favor the slippage of the outermost wire, and thus reduce the load
389 they support. The layers underneath consequently sustain higher stress levels, resulting in more rapid fatigue crack growth.
390 On the other hand, at low Y_b, the wires of the outer layer share a larger part of the total load and are more severely affected
391 by the fatigue crack propagation than the inner layers.
392 Fig. 14 also shows that in all cases, the FE model predicts a first wire break in the inner layer, which is not in perfect
393 agreement with the experimental measurements. On the other hand, it is consistent with the numerical results of Fig. 11b)
394 and c). This difference with the experimental measurements may be explained in part by underestimated friction coefficients
395 (μ_a), especially in the clamped region. Indeed, Fig. 12 shows that higher μ_a tend to increase the outer layer stress, while
396 having less of an effect on the inner ones. The boundary conditions considered in the FE model in lieu of the real shape of the
397 clamping fixture may also affect the outer layer slippage conditions.
398 In addition, the wear damages occurring at inter-wire contact points, which are not explicitly considered within the
399 present fatigue formulation (eq.6), also certainly contribute to the differences between the experimental and numerical life
400 predictions. The prevailing inter-wire contact regime may generate either sticking, gross slip or mixed conditions. While the
401 sticking condition considerably reduces wear phenomena, gross slips lead to important wear rates. Therefore, since wear and
402 fatigue are competing degradation modes, as supported by experimental measurements the mixed conditions associated
403 with lower wear rates and rougher surfaces appears as the most detrimental regime [30]. Therefore, investigations focusing
404 on the identification and the adaptation of a damage criterion better accounting for contact conditions, such as those
405 published in Ref. [32,33], or considering wear laws as in Ref. [14], may contribute to refined the conductor life prediction
406 obtained from the present FE model.
407 Finally, while the developed FE model precision may further be improved (with the addition of the suspension clamps and
408 the incorporation of a refined damage criterion accounting for fatigue-wear interactions), the prediction accuracy remains
409 quite high overall. The numerical results in Fig. 14 compare well with the experimental measurements, as well as with the
410 semi-empirical estimations resulting from the CIGRÉ formula (eq. 6.1). Actually, because the omission of the clamp in the
411 model reduces the calculation times considerably, the modeling strategy presented represents an effective trade-off.

7. Conclusion

The present paper made use of the FE modeling strategy developed in Part I to study the internal strain-stress conditions of ACSR conductors submitted to wind-induced loads. The first portion of the investigation examined the descriptors Y_b and fy_{max} used by researchers and industrial designers to evaluate load severity. The tests directly underlined the discrepancies between these descriptors, along with the difficulty in coupling them in conductor life prediction. The main objective of the second portion of the analysis was to evaluate an alternative way of investigating the conductor fatigue problem based on realistic stress/strain descriptions.

The study included four ACSR covering single- to four-layer configurations. Initial comparisons with reference experimental test data demonstrated the ability of the FE model to predict the bending deflection amplitudes Y_b in the near field of the clamped zone from the far-field vibration parameter fy_{max}.

In order to circumvent the incompatibility existing between Y_b and fy_{max}, and to provide a practical strategy for accurately relating them, a numerical evaluation of their responses integrated into a factorial design approach led to a multivariate prediction equation for Y_b. The resulting model provides instantaneous predictions of Y_b as a function of selected $fy_{max,}$ T and μ_a values within an error level less than 8% when compared to a full 3D FE analysis. Additional comparisons of the predicted Y_b with reference experimental measurements also demonstrated the applicability of the equation to conductors supported by commercial metallic suspension clamps. This simple model offers an easy way of converting and relating reference data established by various laboratories following specific standards and different research goals.

Because the practical descriptions of Y_b and fy_{max} cannot depict the relationship connecting the experimental endurance limit and the strain-stress conditions causing fatigue damages, the study examined the merits of life predictions made from basic stress/strain damage analysis. Disregarding the effect of contact stresses, the investigation only considered the bulk stress/strain amplitudes of the wire to estimate the conductor residual life. Comparisons with experimental data of two multilayered ACSR indicated that the fatigue prediction curves established from the Coffin-Manson fatigue relation provides realistic evaluations of the service life of conductors submitted to both low amplitude deflections generated by wind-induced vibrations and high amplitude deflections resulting from line galloping.

Acknowledgments

This research project was funded by the Natural Sciences and Engineering Research Council (NSERC) of Canada and the Hydro-Quebec/RTE - Structure and mechanics of power transmission lines research chair at Sherbrooke University.

References

[1] Irvine M. Local bending stresses in cables. Int J Offshore Polar Eng 1993;3:172–5.

[2] Raoof M, Davies TJ. End fixity to spiral strands undergoing cyclic bending. J Strain Anal Eng Des 2005;40:129–37.

[3] Zhou ZR, Cardou A, Goudreau S, Fiset M. Fundamental investigations of electrical conductor fretting fatigue. Tribol Int 1996;29:221–32. doi:10.1016/0301-679X(95)00074-E.

[4] EPRI. EPRI Transmission line reference book: Wind-induced conductor motion. Palo Alto, CA: 2006.

[5] Cardou A, Jolicoeur C. Mechanical models of helical strands. Appl Mech Rev 1997;50:1–14.

[6] Lalonde S, Guilbault R, Légeron F. Modeling multilayered wire strands, a strategy based on 3D finite element beam-to-beam contacts - Part I: Model formulation and validation. TBD 2016;TBD:TBD.

[7] Ouaki B, Goudreau S, Cardou A, Fiset M. Fretting fatigue analysis of aluminium conductor wires near the suspension clamp: Metallurgical and fracture mechanics analysis. J Strain Anal Eng Des 2003;38:133–47.

[8] B2.30 CW group. Engineering guidelines relating to fatigue endurance capability of conductor/clamp systems. Cigre Tech Broch No 429 2010:42 p. – 42 p.

[9] Poffenberger JC, Swart RL. Differential displacement and dynamic conductor strain. IEEE Trans Power Appar Syst 1965;PAS-84:508–13.

[10] B2.11.07 CT force. Fatigue endurance capability of conductor / clamp systems: update of present knowledge. Cigre Tech Broch No 332 2007:63 p. – 63 p.

[11] Cardou A. Taut helical strand bending stiffness. UFTscience 2006.

[12] Giglio M, Manes A. Life prediction of a wire rope subjected to axial and bending loads. Eng Fail Anal 2005;12:549–68. doi:10.1016/j.engfailanal.2004.09.002.

[13] Costello GA. Theory of wire rope. 2\superscr ed. New York: Springer-Verlag; 1990.

[14] Argatov II, Gómez X, Tato W, Urchegui MA. Wear evolution in a stranded rope under cyclic bending: Implications to fatigue life estimation. Wear 2011;271:2857–67. doi:10.1016/j.wear.2011.05.045.

[15] Goudreau S, Levesque F, Cardou A, Cloutier L. Strain Measurements on ACSR Conductors During Fatigue Tests II—Stress Fatigue Indicators. IEEE Trans Power Deliv 2010;25:2997–3006. doi:10.1109/TPWRD.2010.2042083.

[16] Cloutier L. Technology watch for gaps in knowledge about conductor fatigue - T083700-3355. Bromont: 2009.

[17] Langlois S, Legeron F, Levesque F. Time History Modeling of Vibrations on Overhead Conductors With Variable Bending Stiffness. IEEE Trans Power Deliv 2013.

[18] Levesque F, Goudreau S, Langlois S, Legeron F. Experimental Study of Dynamic Bending Stiffness of ACSR Overhead Conductors. IEEE Trans Power Deliv 2015;30:2252–9. doi:10.1109/TPWRD.2015.2424291.

[19] Levesque F, Goudreau S, Cardou A, Cloutier L. Strain Measurements on ACSR Conductors During Fatigue Tests I—Experimental Method and Data. IEEE Trans Power Deliv 2010;25:2825–34. doi:10.1109/TPWRD.2010.2060370.

[20] Brunair RM, Ramey GE, Duncan RR. An experimental evaluation of S-N curves and validity of Miner's cumulative damage hypothesis for an ACSR conductor. IEEE Trans Power Deliv 1988;3:1131–40. doi:10.1109/61.193895.

[21] Dalpé C. Interaction mecanique entre conducteur electrique aerien et pince de suspension: Etude sur la fatigue, la rigidite et la fip. Laval University, 1999.

[22] Levesque F, Goudreau S, Cloutier L, Cardou A. Essais en fatigue sur le conducteur ACSR Drake - Rapport No. SM-2006-01. Quebec: 2006.

[23] Jolicoeur C, Goudreau S, Cardou A, Cloutier L. Essais de fatigue d'un conducteur crow avec différentes pinces de suspension sous fortes amplitudes de vibration simulant les conditions de galop - Rapport No. SM-2005-04. Quebec: 2005.

[24] Luc S. Cumul d'endommagement par fatigue d'un conducteur ACSR. Sherbrooke University, 2006.

[25] Levesque F. Etude de l'applicabilite de la regle de Palmgren-Miner aux conducteurs electriques sous chargements de flexion cyclique par blocs. Laval University, 2005.

[26] Cardou A. Stick-slip mechanical models for overhead electrical conductors in bending (with Matlab® applications). Quebec: 2013.

[27] CIGRE Study Committee #22. Endurance capability of conductors. 1988.

[28] Lévesque F, Légeron F. Contact mechanics based fatigue indicator for overhead conductors 2010.

[29] Jolicoeur C, Goudreau S, Cardou A, Cloutier L. Essais en fatigue sur les conducteurs Bersfort et Drake - Rapport No. SM-2001-03. Quebec: 2000.

[30] Zhou ZR, Vincent L. Mixed fretting regime. Wear 1995;181-183:531–6.

[31] Zhou ZR, Cardou A, Fiset M, Goudreau S. Fretting fatigue in electrical transmission lines. Wear 1994;173:179–88.

[32] Szolwinski MP, Farris TN. Mechanics of fretting fatigue crack formation. Wear 1996;198:93–107.

[33] Alfredsson B, Cadario A. A study on fretting friction evolution and fretting fatigue crack initiation for a spherical contact. Int J Fatigue 2004;26:1037–52.